

# Multiple Poincaré sections method for finding the quasiperiodic orbits of the restricted three body problem

Egemen Kolemen · N. Jeremy Kasdin · Pini Gurfil

Received: 12 October 2010 / Revised: 3 May 2011 / Accepted: 16 September 2011  
© Springer Science+Business Media B.V. 2011

**Abstract** A new fully numerical method is presented which employs multiple Poincaré sections to find quasiperiodic orbits of the Restricted Three-Body Problem (RTBP). The main advantages of this method are the small overhead cost of programming and very fast execution times, robust behavior near chaotic regions that leads to full convergence for given family of quasiperiodic orbits and the minimal memory required to store these orbits. This method reduces the calculations required for searching two-dimensional invariant tori to a search for closed orbits, which are the intersection of the invariant tori with the Poincaré sections. Truncated Fourier series are employed to represent these closed orbits. The flow of the differential equation on the invariant tori is reduced to maps between the consecutive Poincaré maps. A Newton iteration scheme utilizes the invariance of the circles of the maps on these Poincaré sections in order to find the Fourier coefficients that define the circles to any given accuracy. A continuation procedure that uses the incremental behavior of the Fourier coefficients between close quasiperiodic orbits is utilized to extend the results from a single orbit to a family of orbits. Quasi-halo and Lissajous families of the Sun–Earth RTBP around the L2 libration point are obtained via this method. Results are compared with the existing literature. A numerical method to transform these orbits from the RTBP model to the real ephemeris model of the Solar System is introduced and applied.

**Keywords** Quasiperiodic orbit · Quasi-halo · Lissajous orbit · Restricted three-body problem · Poincaré section

---

E. Kolemen (✉)  
Princeton Plasma Physics Laboratory, Princeton, NJ, USA  
e-mail: ekolemen@pppl.gov

N. J. Kasdin  
Princeton University, Princeton, NJ, USA

P. Gurfil  
Technion, Israel Institute of Technology, Haifa, Israel

## 1 Introduction

The libration points of the Earth–Moon and Sun–Earth systems have many advantageous properties that render them desirable for space missions, such as a stable thermal environment for infrared space telescopes and continuous coverage of the backside of the Moon for communication with future Moon bases. These properties have enabled existing and planned missions, such as the James Webb Space Telescope and Wilkinson Microwave Anisotropy Probe, among others. With the many future missions planned for these regions, the need for efficient approaches for trajectory design is apparent.

For satellite missions, it is sufficient to consider the Restricted Three Body Problem (RTBP) for the design of these trajectories (Murray and Dermott 2000). In order to minimize station-keeping, periodic orbits are of great interest. Using various methods, Farquhar (1967), Farquhar and Kamel (1973), Hénon (1973), Breakwell and Brown (1979), Howell (1984) and others successfully obtained and studied the three types of periodic orbits around the libration points, namely halo, vertical and horizontal Lyapunov orbits.

Recently, a proposal has been put forward to place a new generation of formation flying missions, such as TPF-I, TPF-O, Con-X, or the New World Observer, in orbits about the Sun–Earth L2 libration point. One way of reducing fuel consumption is to place all of the spacecraft in a constellation stationed on a quasiperiodic orbit, thus maintaining a maximum separation. Because of the large separation distances, however, linear analysis and control is not possible.

There have been a number of studies targeted at finding the quasiperiodic orbits around the libration points. (For background on general mathematical methods concerning the invariant tori, see e.g. Schilder et al. 2005 and references therein.) Howell and Pernicka used an ad hoc shooting method to find the Lissajous orbits (see, e.g. Howell and Pernicka 1988 and references therein). However, the period of the orbit cannot be specified and there is no apparent way of continuation. Being able to specify the period of these orbits are very important for formation flying missions that require all spacecraft to stay close to one another at all times, since an uncontrolled mismatch in this period would lead to large separations. Barden and Howell (1998, 1999) applied this method to find quasi-halos. Jorba and Villanueva (1998) used the normal form method to find the center manifold around libration points. This method can be used to find the quasiperiodic orbits (Jorba and Masdemont 1999), but the periods of the orbits cannot be specified or be based on series expansions; therefore, this method cannot achieve high accuracy. Gómez et al. (1999) used semi-analytic methods based on the Lindstedt-Poincaré procedure to find the quasiperiodic orbits around libration points. A significant drawback of this method is that it has a low radius of convergence, and that a new code must be written for each orbit family. Coding this semi-analytic algorithm is time-consuming and is thus difficult to implement. Gómez and Mondelo used a refined Fourier analysis to find the full families, but this method is very slow and thus must be implemented on a cluster of parallel computers (Gómez and Mondelo 2001; Mondelo 2001).

In this paper we present a novel fully-numerical method for finding quasiperiodic orbits around libration points. Unlike the analytical methods that are often constrained to a particular set of orbits and are cumbersome to implement, the fully-numerical method can be implemented quickly and easily with modest resources. The main advantages of this method are the small overhead cost of programming and very fast execution times, robust behavior near chaotic regions that leads to full convergence for given family of quasiperiodic orbits and the minimal memory required to store these orbits.

The paper is structured as follows: First, an overview of the periodic and quasiperiodic orbits around the libration point is given. Next, the main idea of the numerical procedure

is explained. The methodology is first introduced by explaining the procedure for a single Poincaré section. The results are then extended to multiple Poincaré sections. Different implementations using various Poincaré surfaces are discussed. A continuation method to find the full family of quasiperiodic orbits is introduced. Then, numerical details for obtaining the real quasiperiodic orbits around L2 are explained. A results section follows, wherein the solutions for the quasiperiodic orbits around the L2 point of the RTBP, as well as the Lissajous and the quasi-halo orbits, are given. Finally, the numerical method to “export” these orbits from the RTBP model to a real ephemeris model of the Solar System is explained and applied.

For the sake of conciseness, this paper focuses on the phase space around the Sun–Earth L2 libration point. The results can be straightforwardly extended to other collinear libration points in the Sun–Earth and Earth–Moon systems.

## 2 Families of periodic and quasiperiodic orbits around L2

We employ the synodical frame to define the motion of a massless object (i.e. idealization of a spacecraft) in the RTBP. This is a rotating reference frame defined with the origin at the center of mass of the two primaries,  $m_1$  and  $m_2 < m_1$ , and the following coordinate system:  $x$  is directed from  $m_1$  to  $m_2$ ;  $y$  is perpendicular to  $x$ , positive in the direction of  $m_2$ 's velocity and lies in the plane of the primaries' motion; and  $z$  completes the right-hand coordinate system. Normalizing the distances such that the distance between the primaries is 1, and normalizing time such that the period of the circular motion about the center of mass is  $2\pi$ , we can write the equations of motion as

$$\begin{aligned} \ddot{x} &= 2\dot{y} + x - \frac{(1 - \mu)(x + \mu)}{\|\mathbf{r}_1\|^3} - \frac{\mu(x - 1 + \mu)}{\|\mathbf{r}_2\|^3} \\ \ddot{y} &= -2\dot{x} + y - \frac{(1 - \mu)y}{\|\mathbf{r}_1\|^3} - \frac{\mu y}{\|\mathbf{r}_2\|^3} \\ \ddot{z} &= -\frac{(1 - \mu)z}{\|\mathbf{r}_1\|^3} - \frac{\mu z}{\|\mathbf{r}_2\|^3}, \end{aligned} \tag{1}$$

where  $\mu = \frac{m_2}{m_1+m_2}$ ;  $\|\mathbf{r}_1\|$  and  $\|\mathbf{r}_2\|$  are the distances to  $m_1$  and  $m_2$ , respectively; and the notation  $(\dot{\phantom{x}})$  is used for the time derivative.

Defined by the Eq. (1), the RTBP has a first integral called the *Jacobi constant*,  $C$ , which is given by

$$C = -(\dot{x}^2 + \dot{y}^2 + \dot{z}^2) + 2 \left( \frac{1 - \mu}{\|\mathbf{r}_1\|} + \frac{\mu}{\|\mathbf{r}_2\|} + \frac{x^2 + y^2}{2} \right) + \mu(1 - \mu). \tag{2}$$

The existence of this integral of motion is due to the time-independence of the Lagrangian of the RTBP (see Gómez et al. 2004 for details).

For the purpose of our study, which focuses on the motion around the Sun–Earth/Moon L2, we assume that the Earth/Moon two-body system is a single point mass rotating around the Sun with  $\mu = 3.040423398444176 \times 10^{-6}$  (Gómez et al. 1999).

## 2.1 Periodic orbits

The linear six-dimensional phase space around the Sun–Earth/Moon L2 is of a center  $\times$  center  $\times$  saddle type (Gómez et al. 2000a,b). For Jacobi energy values close to that at L2, where it is sufficient to consider only the linear approximation to the equations of motion, there exist two families of periodic orbits; the horizontal Lyapunov orbits, which are in the ecliptic plane, and the horizontally symmetric figure-eight-shaped vertical Lyapunov orbits. As the energy is increased, and nonlinear terms become important, the linear phase space is broken and a new periodic family, halo orbits, bifurcate from the horizontal Lyapunov orbit family. These orbits are three-dimensional and asymmetric about the ecliptic plane. Figure 1 shows the three distinct periodic orbit families around L2. Note that the Moon's orbit is shown to give a sense of size in these figures. The mentioned periodic orbits only exist in the RTBP (see Section 6 for orbits in the realistic Solar System model).

## 2.2 Quasiperiodic orbits

The four-dimensional center manifold around L2 is occupied by quasiperiodic orbits of two different families as shown in Fig. 2: The Lissajous family around the vertical Lyapunov orbits, and the quasi-halos around the halo orbits. These quasiperiodic orbits reside on invariant tori about the corresponding periodic orbit. To visualize this four-dimensional center manifold on a two-dimensional figure, we need to reduce the center manifold by two dimensions. A convenient way of achieving this is to choose periodic and quasiperiodic orbits which have the same energy, and to take a Poincaré section when these orbits cross the ecliptic plane. The procedure yields Fig. 3. Since this is a Poincaré section, the equilibrium points correspond to periodic orbits of the original system, while the closed curves correspond to the quasiperiodic orbits. This correspondence is shown in Fig. 3. Detailed approaches for obtaining these orbits are discussed in the following sections.

**Fig. 1** Horizontal Lyapunov, vertical Lyapunov and halo periodic orbits around L2 libration point

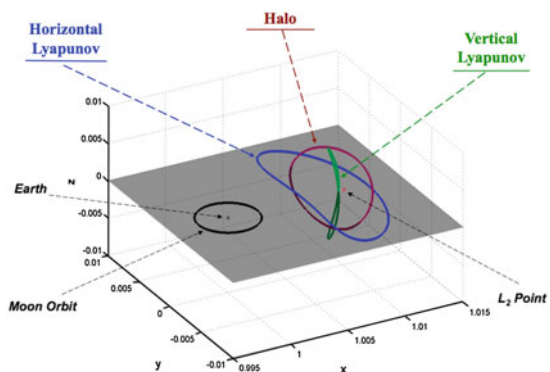


**Fig. 2** Quasiperiodic orbits around the L2 libration point

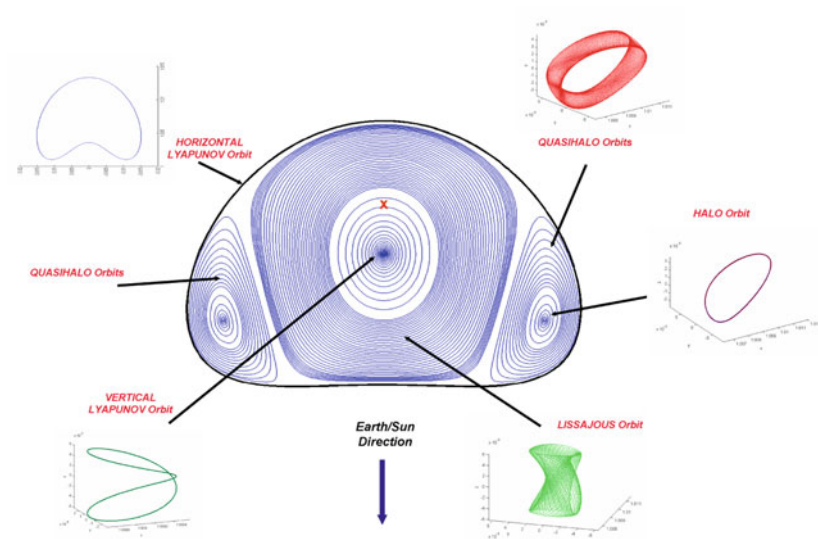
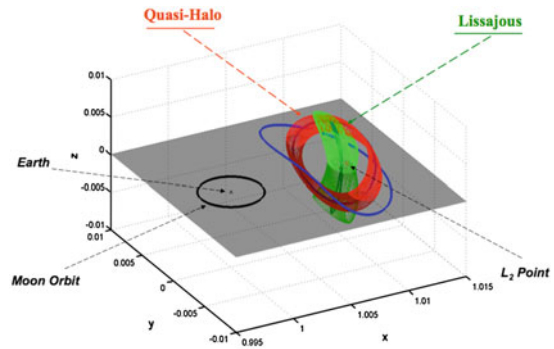


**Fig. 3** Periodic and quasiperiodic orbits around L2 with the same energy shown on a Poincaré section of the ecliptic plane

### 3 Numerical procedure to obtain the quasiperiodic orbits

#### 3.1 Finding invariant tori via a single Poincaré section

For the space-based telescoping missions of interest, the most pertinent quasiperiodic orbits of interest are the quasi-halos, which lie on a two-dimensional invariant manifold. As discussed in the Introduction, the multiple Poincaré section procedure aims to reduce the problem of finding the two-dimensional invariant manifold to finding the invariant circles, i.e., the one-dimensional invariant manifold of the Poincaré map. These invariant circles compactly define the full two-dimensional manifold.

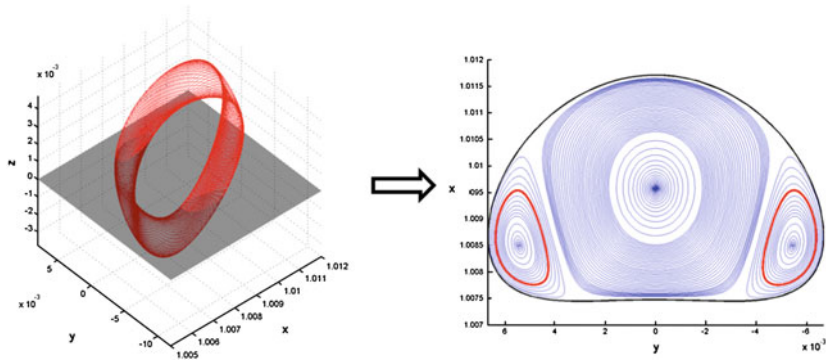


**Fig. 4** Converting the problem of searching for a torus to that of searching for a circle of a map

The first step in the single Poincaré section procedure is to find a convenient Poincaré section. This can be a section in any of the 6-dimensional phase-space coordinates including the position and/or the velocity elements of the state. Figure 4 shows the projection on the position space of a torus and its intersection with a Poincaré section.

When choosing the plane of the section, the main concern is to ensure that the velocity vector of the quasiperiodic orbit be as transverse to the surface of section,  $\Sigma$ , as possible. This reduces the possibility that the integrated points will not return to the Poincaré section. Thus, a good candidate for the Poincaré section is the plane perpendicular to the velocity vector of the halo orbit. For the specific case of the RTBP, another suitable plane-of-section is the ecliptic plane, since the type of quasiperiodic orbits of interest transversely cross this plane. We used both types of Poincaré sections in this paper.

We expand the invariant circle,  $\gamma$ , into a truncated Fourier series with respect to the variable  $\theta \in [0, 2\pi)$ , the angular parameter on the invariant circle:

$$\gamma(\theta) = \frac{\mathbf{a}_0}{\sqrt{2}} + \sum_{n=1}^{n_{max}} [\mathbf{a}_n \cos(n\theta) + \mathbf{b}_n \sin(n\theta)], \tag{3}$$

where  $\mathbf{a}_n$  and  $\mathbf{b}_n$  are the six-dimensional Fourier coefficient vectors.

Here, the choice of the angular parameter,  $\theta$ , is problem-dependent. In the case where the Poincaré section is taken on the ecliptic plane, i.e.,  $z = 0$ , as shown in Fig. 4, an intuitive angular parameter is  $\theta = \tan^{-1}(\frac{y-y_{halo}}{x-x_{halo}})$ , where the subscript “halo” is used for the intersection point of the halo orbit. It is important to note that the system must be parameterized such that every point on the invariant circle is uniquely defined by one value of the parameter,  $\gamma(\theta_i)$ . For invariant circles with complex shapes, other parameters, such as the ratio of the arc length between a specific point on the circle and the full arc length of the closed orbit (Kevrekidis et al. 1985), should be used to ensure uniqueness. For the quasiperiodic orbits studied in this paper, however, this simple parameter gives satisfactory results.

We then discretize  $\gamma$ , taking  $N$  points on the invariant circle by choosing a set of angular parameters in the interval  $[0, 2\pi)$ ,

$$\theta_0(i) = \frac{2\pi i}{N} \quad i = 0, 1, \dots, N-1. \tag{4}$$

Every point on this circle also corresponds to a unique element of the torus. We can use the scalar  $\theta_0(i)$  to identify this element of the torus, a six-dimensional (three corresponding to

the position space coordinates and the other three to the velocity space coordinates) vector,  $\mathbf{x}_i$ , in the phase space:

$$\mathbf{x}_i = \frac{\mathbf{a}_0}{\sqrt{2}} + \sum_{n=1}^{n_{max}} [\mathbf{a}_n \cos(n\theta_0(i)) + \mathbf{b}_n \sin(n\theta_0(i))]. \tag{5}$$

Concatenating the  $\mathbf{x}_i$  vectors yields a  $6N$ -dimensional vector,  $\mathbf{X}_0(\theta_0) = \{\mathbf{x}_0, \mathbf{x}_1, \dots, \mathbf{x}_{N-1}\}^T$ , so that:

$$\mathbf{X}_0 = A_{\theta_0} \mathbf{Q}, \tag{6}$$

where  $\mathbf{Q}$  is the  $6 \times (2n_{max} + 1)$ -dimensional concatenated truncated Fourier coefficients vector defined as  $\mathbf{Q} = \{\mathbf{a}_0, \mathbf{a}_1, \mathbf{b}_1, \dots, \mathbf{a}_{n_{max}}, \mathbf{b}_{n_{max}}\}^T$ , and  $A$  is the discrete Fourier matrix that transforms Fourier coefficients to coordinate variables. Subscript of  $A$  shows the angle parameter used. We map these points by integrating the equations of motion until they intersect the Poincaré section again:

$$\mathbf{X}_\tau = \mathbf{P}(\mathbf{X}_0) = \phi(\tau(\mathbf{X}_0), \mathbf{X}_0). \tag{7}$$

Here,  $\tau(\mathbf{X}_0)$  is the time it takes for a given set of points,  $\mathbf{X}_0$ , to reach the Poincaré section,  $\Sigma$ . The notation  $\phi(t, x_0)$  is used for the flow of an ODE from a given initial condition,  $x_0$ , for the specified time interval,  $t$ . The first variations of these equations are integrated along with  $\mathbf{X}_0$  for later use in the iteration process.

Since every point that starts on an invariant map will remain there, if all the mapped points,  $\mathbf{X}_\tau$ , fall exactly on the estimated invariant circle, then the initial guess for the invariant circle is accurate. This condition can be written in mathematical terms as a root finding problem:

$$F(\mathbf{Q}) = \mathbf{X}_\tau - A_{\theta_\tau} \mathbf{Q} = \mathbf{0}. \tag{8}$$

Here,  $\theta_\tau$  defines the projected angular position of  $\mathbf{X}_\tau$  as shown in Fig. 5. It is found by projecting each mapped point,  $\mathbf{X}_\tau$ , onto the invariant circle, then finding the corresponding angle for this point by solving the Fourier expansion Eq. (5) for  $\theta$ . Details of how to obtain it are described in detail in Sect. 4.3.  $A_{\theta_\tau}$  is the Fourier coefficient matrix, which has the same structure as  $A_{\theta_0}$ , but uses the projected angle elements instead of the original ones.

Thus, the problem of finding the quasiperiodic orbit is converted to that of finding the Fourier coefficient vector,  $\mathbf{Q}$ , which solves Eq. (8). It is possible to set up an iterative numerical scheme in order to find the correct parameterization of the quasiperiodic orbit, employing the minimization

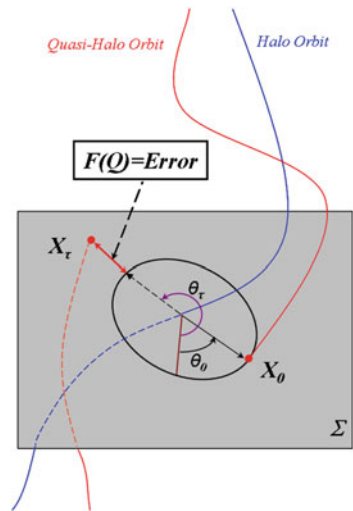
$$\min_{\mathbf{Q}} \|F(\mathbf{Q})\|^2. \tag{9}$$

The schematic illustration of this numerical scheme is shown in Fig. 5, where the error vector to be minimized, i.e., the distance between the mapped points  $\mathbf{X}_\tau$  and the invariant circle, is expressed.

One advantage of this formulation is that it can be solved numerically by a Newton iteration, which has the potential to lead to quadratically-convergent solutions with good initial guesses. The process of identifying these initial guesses will be discussed later. In Newton's iteration, an initial guess  $\mathbf{Q}^0$  is iterated according to

$$DF(\mathbf{Q}^j) (\mathbf{Q}^{j+1} - \mathbf{Q}^j) = -F(\mathbf{Q}^j) \tag{10}$$

**Fig. 5** Schematic illustration of the numerical procedure for finding the invariant torus



until a satisfactory solution is reached. Here,  $DF$  is the gradient of  $F$  with respect to  $\mathbf{Q}$ , and the superscript defines the value of  $\mathbf{Q}$  at a given iteration step.

In order to find an explicit form for this equation, all the variables are expanded in terms of  $\mathbf{Q}$ , so that

$$\begin{aligned}
 F(\mathbf{Q}) &= \mathbf{X}_\tau - \mathbf{X}_{\theta_\tau} \\
 &= \phi(\tau, A_{\theta_0}, \mathbf{Q}) - A_{\theta_\tau} \mathbf{Q}.
 \end{aligned}
 \tag{11}$$

We then take the derivative with respect to  $\mathbf{Q}$ :

$$\begin{aligned}
 DF(\mathbf{Q}) &= \frac{dX_\tau}{dX_0} \frac{dX_0}{dQ} - \frac{\partial X_{\theta_\tau}}{\partial Q} - \frac{\partial X_{\theta_\tau}}{\partial \theta_\tau} \frac{d\theta_\tau}{dX_\tau} \frac{dX_\tau}{dX_0} \frac{dX_0}{dQ} \\
 &= DP A_{\theta_0} - A_{\theta_\tau} - \frac{\partial X_{\theta_\tau}}{\partial \theta_\tau} \frac{d\theta_\tau}{dX_\tau} DP A_{\theta_0},
 \end{aligned}
 \tag{12}$$

where  $DP$  is the differential of the Poincaré map defined in Sect. 4 along with  $\frac{\partial X_{\theta_\tau}}{\partial \theta_\tau}$  and  $\frac{d\theta_\tau}{dX_\tau}$ .

### 3.2 Finding a unique orbit: specifying two additional orbit properties

The quasiperiodic orbits reside in a six-dimensional phase space, which has a four-dimensional center manifold (periodic subspace). Each quasiperiodic orbit is of dimension two. Thus, two properties of a given quasiperiodic orbit must be specified in order to uniquely define it. Many different parameters can be used to specify a quasiperiodic orbit; among these, the most intuitive and relevant for mission design are the Jacobi constant, the period, and the size of the orbit. Prescribing the period also determines the Jacobi constant and vice versa. We therefore consider two different implementation methods, one using the Jacobi constant and another using the orbital period.

When the Jacobi constant is used to specify a quasiperiodic orbit, another constraint is needed in order to define the properties of the orbit of interest. We chose to specify the size of the orbit as the second variable. This is a relevant parameter because the distance between the spacecraft in a formation is set by the size of the quasi-halo orbit.

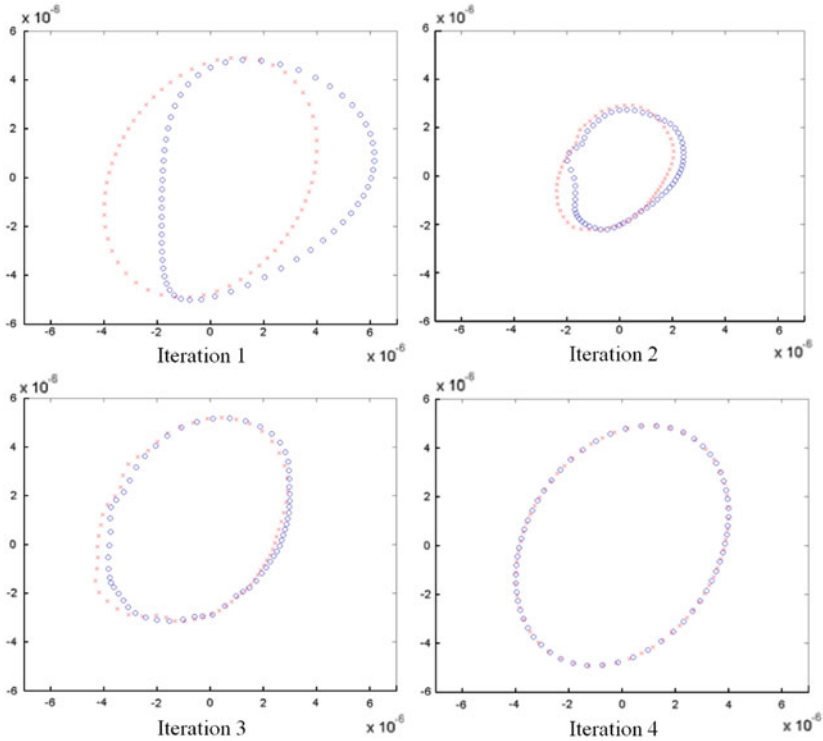


**Fig. 6** Iteration procedure in steps

Since the numerical method is based on Poincaré sections, size can be specified by the two-dimensional area,  $\mathbb{A}$ , which is enclosed by the invariant circle. Then, the constraint vector is augmented to include the new constraints:

$$F = [F ; C_{fixed} - C_Q ; \mathbb{A}_{fixed} - \mathbb{A}_Q]. \tag{13}$$

where the subscripts “fixed” and “Q” are used for the user-specified and algorithm obtained values, respectively.

With these additional constraints we can employ Newton’s iteration given in Eq. (10) to find the unique quasiperiodic orbit we are looking for (see Sect. 4 for details). Solutions converge usually within 3–4 iterations. An example of an iteration procedure is shown in Fig. 6, where the sample points are shown as crosses and the return maps are represented by circles. After four iterations, all the sample points and the return maps are aligned on the same invariant circle.

Another option is to fix the period of the quasiperiodic orbit. Quasi-halo orbits have two periods; one around the halo orbit and the other along the halo orbit. The period along the halo orbit is very important for space missions that require all spacecraft to stay close to one another at all times. An uncontrolled mismatch in this period would lead to a separation on the order of the size of the halo orbit, which is unacceptable. However, this period for a numerically computed two-dimensional structure is vague, unlike the one-dimensional case.

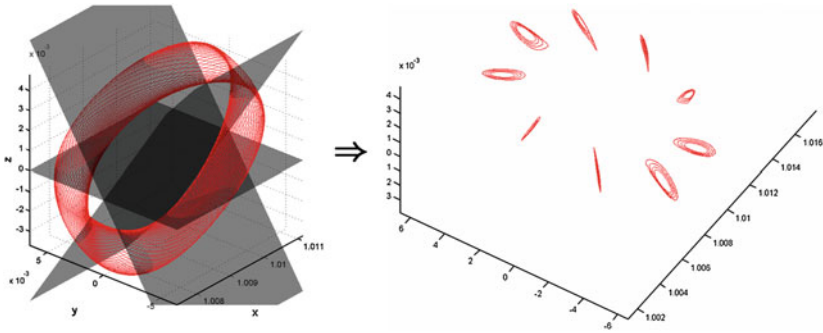


**Fig. 7** Multiple Poincaré section procedure: invariant circles obtained by sectioning the invariant tori

We define this period of the quasi-halo to be the average time it takes for all the sample points starting from the initial Poincaré section to return back to it. That is, the period is

$$T = \frac{1}{n} \sum_{i=1}^n \tau(\mathbf{x}_i). \tag{14}$$

Here,  $n$  is the total number of sample points taken on the Poincaré section. This way, the period of the quasiperiodic orbit can be specified along with the integration direction for the return map. In this case, there is one more degree of freedom required to specify a unique orbit. Choosing the Jacobi constant as a constraint is not an option, as discussed before. Thus, we specify the size of the orbit by choosing the area parameter: the two-dimensional area,  $\mathbb{A}$ , which is enclosed by the invariant circle. This can be achieved by augmenting the error vector with a new constraint, such as the projected size along one direction:

$$F = [F ; T_{fixed} - T_{\mathbf{Q}}; \mathbb{A}_{fixed} - \mathbb{A}_{\mathbf{Q}}]. \tag{15}$$

### 3.3 Extension to multiple Poincaré sections

In order to overcome the potential instability that results from the long integration times, the invariant torus is cut by several Poincaré sections, as mentioned before. Figure 7 shows the invariant circles obtained when the tori of interest are intersected using multiple sections. As a result, all the invariant circles in Fig. 7 are determined, instead of only a single one, as was the case in the previous section.

The numerical procedure is similar to the single Poincaré section method. This time, the sample points are integrated until they hit the next Poincaré section, rather than being integrated for the whole period. For all these invariant circles to lie on the same invariant torus, all the mapped points must be aligned with the invariant circles of the next Poincaré section. The closure of the mathematical problem is obtained by requiring that the sample points from the last Poincaré section map to the first invariant circle. Mathematically, the invariance condition for the invariant circles can be expressed in the same form as in the single Poincaré section case by letting  $\mathbf{Q}$ , the vector containing the Fourier coefficients, be the concatenation of  $\mathbf{q}_i$ , the Fourier coefficients of each of the invariant circles,

$$\mathbf{Q} = [\mathbf{q}_1; \mathbf{q}_2; \dots; \mathbf{q}_{N_p-1}; \mathbf{q}_{N_p}], \tag{16}$$

where  $N_p$  is the number of Poincaré sections.

Thus, the invariance condition for all the invariant circles parameterized by  $\mathbf{q}_i$  to be on the same torus is

$$F(\mathbf{Q}) = \begin{pmatrix} \phi(\tau, A_{\theta_0} \mathbf{q}_1) \\ \phi(\tau, A_{\theta_0} \mathbf{q}_2) \\ \vdots \\ \phi(\tau, A_{\theta_0} \mathbf{q}_{N_p-1}) \\ \phi(\tau, A_{\theta_0} \mathbf{q}_{N_p}) \end{pmatrix} - \begin{pmatrix} A_{\theta_{\phi(\tau, A_{\theta_0} \mathbf{q}_1)}} \mathbf{q}_2 \\ A_{\theta_{\phi(\tau, A_{\theta_0} \mathbf{q}_2)}} \mathbf{q}_3 \\ \vdots \\ A_{\theta_{\phi(\tau, A_{\theta_0} \mathbf{q}_{N_p-1})}} \mathbf{q}_{N_p} \\ A_{\theta_{\phi(\tau, A_{\theta_0} \mathbf{q}_{N_p})}} \mathbf{q}_1 \end{pmatrix} \tag{17}$$

Finally, as before, we apply Newton’s iteration to the root finding problem:

$$DF(\mathbf{Q}^j) (\mathbf{Q}^{j+1} - \mathbf{Q}^j) = -F(\mathbf{Q}^j). \tag{18}$$

### 3.4 Continuation procedure

Once the Fourier coefficients for a given orbit have been obtained, it is important to extend these results to find the complete quasiperiodic family. This procedure is called *continuation*. In this study, we used the area variable,  $\mathbb{A}$ , as the continuation parameter.

While there is no intuitive way to continue the coordinate variables,  $\{x, y, z, \dot{x}, \dot{y}, \dot{z}\}$ , the continuation of the Fourier coefficients is straightforward, since they vary incrementally between sufficiently close quasiperiodic family members. A low-order polynomial fit is thus sufficient for continuing these parameters. Even a very simple linear continuation in the area variable,  $\mathbb{A}$ , gives satisfactory results:

$$\mathbf{Q}_{k+1}^0 = \mathbf{Q}_k + \frac{\mathbb{A}_{k+1} - \mathbb{A}_k}{\mathbb{A}_k - \mathbb{A}_{k-1}} (\mathbf{Q}_k - \mathbf{Q}_{k-1}). \tag{19}$$

Here, as before, the superscript of  $\mathbf{Q}$  defines the Newton iteration step, while the subscript defines the continuation step.

Once the initial guess for  $\mathbf{Q}_{k+1}^0$  is obtained, the multiple Poincaré section method is applied on this guess to get the correct  $\mathbf{Q}_{k+1}$ . Then, the continuation is repeated to find  $\mathbf{Q}_{k+2}$ .

## 4 Numerical application for the quasiperiodic orbits around L2

Algorithm 1 shows the numerical procedure implemented on a computer. The details of the computations are discussed in the sections that follow.

### 4.1 Initial estimate for $\mathbf{Q}$

Let us consider the monodromy matrix,  $M$ , as a linear map from the initial variations around the periodic orbit at time 0 to variation after one period  $T$ ,

$$M := \delta x_0 \rightarrow \delta x_T. \tag{20}$$

Recall that the monodromy matrices for vertical Lyapunov and halo orbits each has an eigenvalue couple,  $\cos \sigma \pm i \sin \sigma$  with modulus 1 and corresponding eigenvector  $\mathbf{v}_1 \pm i \mathbf{v}_2$ . Fundamental properties of eigenvalue and eigenvector for  $M$  can be written as,

**Algorithm 1** Compute the full quasiperiodic orbit family

---

Compute the initial guess:  $\mathbf{Q}_0^0$  and  $\mathbb{A}_0$   
 $k \leftarrow 0, \quad c = 1.2$   
**while**  $\mathbb{A}_k < \mathbb{A}_{max}$  **do**  
    $j \leftarrow 0, \quad flag = 0$   
   **while**  $flag = 0$  **do**  
     1. Compute  $X_0$   
        $\mathbf{X}_0 = A_{\theta_0} \mathbf{Q}_k^j$   
     2. Compute a Poincaré map for each  $\Sigma_i$   
        $\mathbf{X}_\tau = P(\mathbf{X}_0)$   
     3. Compute the projected angle  
        $\theta_{\mathbf{X}_\tau} = \tan^{-1} \left( \frac{X_\tau(2)}{X_\tau(1)} \right)$  for Lissajous orbits  
        $\theta_{\mathbf{X}_\tau} = \tan^{-1} \left( \frac{X_\tau(6)}{X_\tau(5)} \right)$  for quasi-halo orbits  
     4. Compute the error:  
        $F(\mathbf{Q}_k^j) = \mathbf{X}_\tau - A_{\theta_{\mathbf{X}_\tau}} \mathbf{Q}_k^j$   
     5. Compute the Jacobian of the error:  
        $DF(\mathbf{Q}_k^j) = DP A_{\theta_0} - A_{\theta_\tau} - \frac{\partial X_{\theta_\tau}}{\partial \theta_\tau} \frac{d\theta_\tau}{dX_\tau} DP A_{\theta_0}$   
     6. Augment the error vector and the Jacobian  
        $F = [F; \mathbb{A}_k - \mathbb{A}_Q; \dots], \quad DF = [DF; D\mathbb{A}; \dots]$   
     7. Perform a Newton iteration  
        $DF(\mathbf{Q}_k^j) (\mathbf{Q}_k^{j+1} - \mathbf{Q}_k^j) = -F(\mathbf{Q}_k^j)$   
     8.  $j \leftarrow j + 1$   
     **if**  $|F| < \epsilon$  **then**  
        $flag = 1, \quad \mathbf{Q}_k = \mathbf{Q}_k^j, \quad k \leftarrow k + 1$   
     **else if**  $j = j_{max}$  **then**  
        $flag = 2, \quad c = 1.0, \quad \Delta\mathbb{A} = 0.8\Delta\mathbb{A}$   
     **end if**  
   **end while**  
    $\mathbb{A}_k = \mathbb{A}_{k-1} + c \Delta\mathbb{A}$   
   **Continuation:** Extrapolate an initial guess for  $\mathbf{Q}_k^0$   
      $\mathbf{Q}_k^0 = polyfunc(\mathbb{A}_k)$   
   **end while**

---

$$\begin{aligned}
 M(\mathbf{v}_1 + i\mathbf{v}_2) &= (\cos \sigma + i \sin \sigma) (\mathbf{v}_1 + i\mathbf{v}_2) \\
 &= \cos \sigma \mathbf{v}_1 - i \sin \sigma \mathbf{v}_2 + i(\sin \sigma \mathbf{v}_1 + \cos \sigma \mathbf{v}_2), \quad (21)
 \end{aligned}$$

$$\begin{aligned}
 M(\mathbf{v}_1 - i\mathbf{v}_2) &= (\cos \sigma - i \sin \sigma) (\mathbf{v}_1 - i\mathbf{v}_2) \\
 &= \cos \sigma \mathbf{v}_1 - i \sin \sigma \mathbf{v}_2 - i(\sin \sigma \mathbf{v}_1 + \cos \sigma \mathbf{v}_2). \quad (22)
 \end{aligned}$$

Using these properties, it is possible to find the invariant circle of the map  $M$ . Let us consider a closed curve,  $\varphi$ , of this map, parameterized by  $\theta = [0, 2\pi]$  and magnitude of  $\kappa$ ,

$$\varphi(\theta) = \kappa(\cos \theta \mathbf{v}_1 - \sin \theta \mathbf{v}_2). \quad (23)$$

Using trigonometric manipulations, it can be shown that the monodromy matrix maps this closed curve onto itself with an angle shift,  $\rho$ :

$$\begin{aligned}
 \varphi(\theta) &\xrightarrow{M} M \kappa(\cos \theta \mathbf{v}_1 - \sin \theta \mathbf{v}_2) \\
 &= \kappa[\cos(\theta + \rho) \mathbf{v}_1 - \sin(\theta + \rho) \mathbf{v}_2] \\
 &= \varphi(\theta + \rho). \quad (24)
 \end{aligned}$$

Thus,  $\varphi(\theta)$  is a periodic orbit of this map (which should not be confused with the invariant circle of the Poincaré section) with magnitude  $\kappa$ . It is a linear approximation of the relative distance from the quasiperiodic orbit to the periodic orbit.

In the numerical scheme, we used the linear approximation with small  $\kappa$  as the starting point for the multiple Poincaré scheme.  $\kappa$  values of order  $10^{-6}$  have been sufficiently small to give reasonable initial approximations (recall that, in normalized units, 1 is the distance between the Sun and the Earth).

$\varphi(\theta)$  is a periodic orbit of the monodromy map. We first choose a large number (e.g.  $N_M = 100$ ) of parametrization variables,

$$\theta_M(i) = \frac{2\pi i}{N_M} \quad i = 0, 1, \dots, N_M - 2, N_M - 1, \tag{25}$$

and obtain the corresponding  $N_M$  points on the closed curve:

$$\mathbf{X}_M = \varphi(\theta_M). \tag{26}$$

For the multiple Poincaré sections algorithm, an initial estimate is needed for the periodic orbit on the Poincaré map. To this aim, we integrated the variables  $\mathbf{X}_M$  and found their intersection with the Poincaré sections of interest. The method employed is the subject of the two sections that follow.

The initial estimate for the Fourier elements,  $\mathbf{Q}_0^0$ , was obtained by using a fast Fourier transform (FFT) on the intersecting points. It is important to note that this is the only time that a Fourier transform is employed in the algorithm. Once  $\mathbf{Q}_0^0$  is obtained, all the transformations, including the continuation step, take  $\mathbf{Q} \rightarrow \mathbf{X}$ . For ease of programming, we chose to use real-valued Fourier coefficients rather than imaginary ones. In Algorithm 2, a pseudo-code shows how to obtain the Fourier coefficients ( $i_{max} = 20$ ). Since  $\sin(0) = 0$ , the imaginary part of  $y(1)$  is always 0.

---

**Algorithm 2** Compute  $\mathbf{Q}$ , real Fourier coefficients vector

---

```

input: X
N= length(X);
y = fft(X);
Q(1) = 1/sqrt(2)/N*real(y(1));
for i=2 : i_max do
    Q(2*(i-1))= 2/N*real(y(i));
    Q(2*(i-1)+1)= -2/N*imaginary(y(i));
end for
output: Q
    
```

---

#### 4.2 Choosing the Poincaré section surfaces

For the Lissajous orbits, we restrict the Poincaré sections to be on one side of the ecliptic (i.e.  $z = 0$ ) plane because of the mirror symmetry of the RTBP dynamics with respect to the  $z$  plane. For the single Poincaré section method, we used a section on the ecliptic plane. When extending this to multiple Poincaré sections, an intuitive choice was to use sections parallel to  $z = 0$ . Thus, we chose four sections,  $g_i(\mathbf{x})$  corresponding to  $i = 1 : 4$ , over the half period (equivalent to seven sections over the full period). Two of these are  $z = 0$  and the other two are  $z = z_{fixed}$ , one section as the trajectories cross these sections in one direction and another while they cross in the other direction:

$$0 = g_i(\mathbf{x}) = z_{fixed_i} - z_{li}(\tau_i) \quad (27)$$

where the subscript  $li$  stands for the Lissajous orbit. We chose  $z_{fixed}$  to be half of the maximum displacement in the  $z$ -direction to ensure that all the trajectories are transversal.

For quasi-halos, sections that are parallel to one another cannot be considered, since the torus twists in space. A good candidate for the Poincaré section surface,  $g(\mathbf{x})$ , is the plane perpendicular to the velocity of the halo orbit section:

$$0 = g_i(\mathbf{x}) = [x_h(t_i) - x_{qh}(\tau_i)]\dot{x}_h + [y_h(t_i) - y_{qh}(\tau_i)]\dot{y}_h + [z_h(t_i) - z_{qh}(\tau_i)]\dot{z}_h, \quad (28)$$

where the subscript  $h$  stands for the halo orbit and the subscript  $qh$  stands for the quasi-halo orbit.

Along the quasi-halo, ten of these sections,  $g_{i=0\dots 9}$ , are taken with equal separation in time, i.e.,  $t_i = \frac{i}{9T}$ , where  $i = 0, \dots, 9$ . Figure 7 shows the multiple Poincaré sections on a sample quasi-halo orbit. Then, the Fourier coefficients that correspond to all the sections along the trajectory are continued, giving initial conditions to the next quasi-halo.

#### 4.3 Choosing $\theta$ and computing the derivative $\frac{d\theta \mathbf{x}_\tau}{dX_\tau}$

We choose the Poincaré sections to be along the coordinate variables of the state. Thus, an intuitive choice for  $\theta$  would be to pick it as the angle between the coordinate variables of the invariant circles. Since all the sections,  $g_i(\mathbf{x}) = z_{fixed_i} - z_{qh}(\tau_i)$ , for the Lissajous case are parallel to one another, it is feasible to choose  $\theta$  as the angle between the coordinate variables  $\theta = \tan^{-1}(y/x)$ . A single form of parametrization,  $\theta = \tan^{-1}(y/x)$ , defines the cross sections on all the Poincaré sections uniquely, and this is therefore the parametrization that we use.

A major advantage of such a parametrization is the reduction in the size of  $\mathbf{Q}$ . Since  $z$  is constant on the Poincaré section, the Fourier coefficient is not needed for this vector. In addition, an explicit interdependence of  $x$  and  $y$  makes it feasible to use one Fourier element vector to define both these states. Thus, instead of using six sets of Fourier element vectors to define six states, it can be reduced to four sets. The reduced Fourier series vector is

$$\mathbf{Q} = \left[ \mathbf{Q}_R^T, \mathbf{Q}_x^T, \mathbf{Q}_y^T, \mathbf{Q}_z^T \right]^T, \quad (29)$$

where  $R = \sqrt{x^2 + y^2}$  and  $\mathbf{Q}_R, \mathbf{Q}_x, \mathbf{Q}_y, \mathbf{Q}_z$  are the Fourier series coefficients of the  $R, \dot{x}, \dot{y}, \dot{z}$ , variables of the invariant circle, respectively.

Unlike the Lissajous case, the Poincaré sections given in Eq. (29) are not parallel in the case of the quasi-halo orbits. The choice of  $\theta$  as the angle along the coordinate variables leads to different parameterizations for each of the sections. In order to reduce the extra complication that this would entail, we opted for a simpler parametrization that works for all the sections at the same time, as in the Lissajous case. Figure 8 shows the projection of the invariant circle on different axes of all the closed orbits on the Poincaré sections. Looking at this figure, it is apparent that the parameterization  $\theta = \tan^{-1}(\dot{z}/\dot{y})$  works for all the sections. As with the Lissajous case, a major advantage of such a parametrization is the reduction in size of  $\mathbf{Q}$ . The reduced Fourier series vector for a quasi-halo is thus

$$\mathbf{Q} = [\mathbf{Q}_x^T; \mathbf{Q}_y^T; \mathbf{Q}_z^T; \mathbf{Q}_x^T; \mathbf{Q}_R^T], \quad (30)$$

where  $R = \sqrt{\dot{y}^2 + \dot{z}^2}$  and  $\mathbf{Q}_x, \mathbf{Q}_y, \mathbf{Q}_z, \mathbf{Q}_x, \mathbf{Q}_R$  are the Fourier series coefficients of the  $x, y, z, \dot{x}, R$  variables of the invariant circle, respectively.

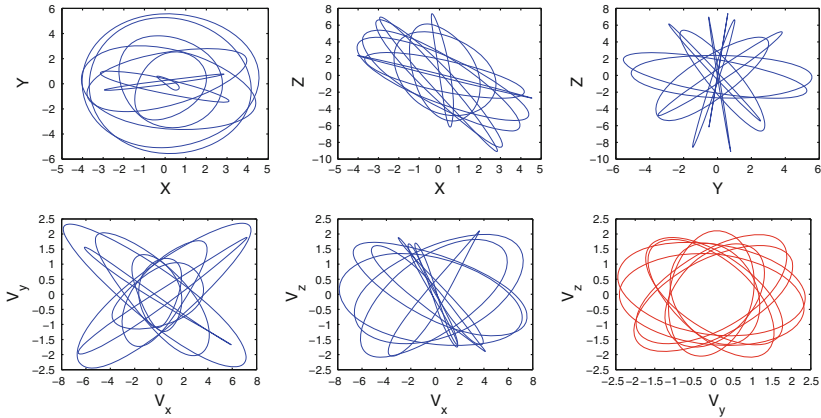


**Fig. 8** The relative distance from the invariant circle is projected on different axes for a sample orbit. The *upper* three sub-plots show the projection on the position space, while the *lower* ones show the projection on the velocity space. The sub-plot on the lower right corner, which is the  $V_y$  (i.e.  $\dot{y}$ ) versus  $V_z$  (i.e.  $\dot{z}$ ), is highlighted in red

Finally, employing the chain rule, the derivative of  $\theta$  with respect to  $\mathbf{X}_\tau$  can be obtained as

$$\begin{aligned} \frac{d\theta_{\mathbf{X}_\tau}}{dX_\tau} &= \left[ -\frac{y}{x^2 + y^2}, \frac{x}{x^2 + y^2}, 0, 0, 0, 0, \right] && \text{for Lissajous} \\ \frac{d\theta_{\mathbf{X}_\tau}}{dX_\tau} &= \left[ 0, 0, 0, 0, -\frac{\dot{z}}{\dot{y}^2 + \dot{z}^2}, \frac{\dot{y}}{\dot{y}^2 + \dot{z}^2} \right] && \text{for quasi-halo.} \end{aligned}$$

#### 4.4 Computing $A_\theta$ and $\frac{\partial X_{\theta_\tau}}{\partial \theta_\tau}$

Recall that the invariant circle on the Poincaré section,  $\gamma$ , was defined via a finite Fourier series with  $\theta$  on the interval  $[0, 2\pi)$  in Eq. (3) and  $A_\theta$  is the transformation from these Fourier elements to the state vector.

In this section, we explain how to obtain this matrix and its derivative. The Fourier coefficients vector,  $\mathbf{Q}$ , for Lissajous and quasi-halo orbits was defined in Eqs. (29) and (30). The state vector,  $\mathbf{X}$ , can then be obtained by multiplying  $\mathbf{Q}$  by the following  $A_\theta$ :

$$A_\theta = \begin{bmatrix} A_{section_1} & 0 & \cdots & 0 & 0 \\ 0 & A_{section_2} & \cdots & 0 & 0 \\ \vdots & \vdots & \ddots & 0 & 0 \\ 0 & 0 & 0 & A_{section_{N_p-1}} & 0 \\ 0 & 0 & 0 & 0 & A_{section_{N_p}} \end{bmatrix}. \tag{31}$$

In the above equation, the maximum number of sections,  $N_p$ , is four for Lissajous orbits and ten for quasi-halo orbits, and

$$A_{\text{section}_i} = \begin{bmatrix} A_1 \\ A_2 \\ \vdots \\ A_{N_{\text{npoints}}-1} \\ A_{N_{\text{npoints}}} \end{bmatrix}, \quad (32)$$

where  $N_{\text{npoints}} = 40$  is the number of points on each Poincaré section. Defining the  $2n_{\text{max}} + 1$  dimensional vector

$$cs(\theta_i) = \left[ \frac{1}{2} \cos(\theta_i) \sin(\theta_i) \cos(2\theta_i) \sin(2\theta_i) \cdots \cos(n_{\text{max}}\theta_i) \sin(n_{\text{max}}\theta_i) \right], \quad (33)$$

where  $n_{\text{max}} = 20$  is the maximum number of Fourier elements introduced in Eq. (5) and recalling that  $x = R \cos(\theta)$ ,  $y = R \sin \theta$  and  $z = 0$  on the Lissajous Poincaré section, the  $6 \times (8n_{\text{max}} + 4)$  dimensional  $A_i$  matrix for Lissajous orbits is given by

$$A_i = \begin{bmatrix} \cos(\theta_i)cs(\theta_i) & 0 & 0 & 0 \\ \sin(\theta_i)cs(\theta_i) & 0 & 0 & 0 \\ 0 & 0 & 0 & 0 \\ 0 & cs(\theta_i) & 0 & 0 \\ 0 & 0 & cs(\theta_i) & 0 \\ 0 & 0 & 0 & cs(\theta_i) \end{bmatrix}. \quad (34)$$

Note that the constant value of  $z_{\text{fixed}}$  has to be added to  $A_{\theta}$   $\mathbf{Q}$  later on. Recall that for  $\dot{y} = R \cos(\theta)$ ,  $\dot{z} = R \sin \theta$  for the quasi-halo Poincaré section, thus the  $6 \times (10n_{\text{max}} + 5)$  dimensional  $A_i$  for this case becomes

$$A_i = \begin{bmatrix} cs(\theta_i) & 0 & 0 & 0 & 0 \\ 0 & cs(\theta_i) & 0 & 0 & 0 \\ 0 & 0 & cs(\theta_i) & 0 & 0 \\ 0 & 0 & 0 & cs(\theta_i) & 0 \\ 0 & 0 & 0 & 0 & \cos(\theta_i)cs(\theta_i) \\ 0 & 0 & 0 & 0 & \sin(\theta_i)cs(\theta_i) \end{bmatrix}. \quad (35)$$

$\frac{\partial X_{\theta_\tau}}{\partial \theta_\tau}$  can be obtained in a similar fashion. For conciseness, we do not include the explicit form of  $\frac{\partial X_{\theta_\tau}}{\partial \theta_\tau}$ . It can be obtained via term-by-term differentiation of  $A_{\theta_\tau}$   $\mathbf{Q}$ .

#### 4.5 Augmenting the error vector, $\mathbf{F}$ , and its derivative $D\mathbf{F}$

One of the main advantages of this algorithm is the ease with which constraints can be added. For example, in order to fix the value of the Jacobi constant, Eq. (13) is used to augment the error vector, where  $C_{\text{fixed}}$  is set to the Jacobi constant of the base halo or the vertical Lyapunov orbit.

As for the determination of the area variable,  $\mathbb{A}$ , using the Fourier coefficients is of great utility. If  $R$  denotes the region enclosed by a curve  $r(\theta)$  and the rays  $\theta = a$  and  $\theta = b$ , where  $0 < b - a \leq 2\pi$ , the area of  $R$  is

$$\mathbb{A} = \frac{1}{2} \int_a^b r(\theta)^2 d\theta. \quad (36)$$

Substituting the Fourier expansion in Eq. (3) for  $r(\theta)$ , and noting that  $a = 0, b = 2\pi$  and  $r(0) = r(2\pi)$ , the well-known Parseval theorem (Rayleigh 1806) states that the area integral becomes

$$\mathbb{A} = \frac{\pi}{2} \langle \mathbf{Q}_R, \mathbf{Q}_R \rangle, \tag{37}$$

where  $\langle . . . \rangle$  is the usual inner product.

For the fixed period case, the augmentation given in Eq. (15) is used to obtain the error vector, where  $T_{fixed}$  is set to the period of the base halo or the vertical Lyapunov orbit. The period of quasiperiodic orbit,  $T$ , is obtained from Eq. (14).

As for the derivative terms, the gradient of the Jacobi constant is

$$DC = \nabla_x C DP A_{\theta_0}, \tag{38}$$

where

$$\nabla_x C = \begin{bmatrix} 2x + \frac{-2\mu(-1 + \mu + x)}{(-1 + \mu + x)^2 + y^2 + z^2)^{3/2}} - \frac{2(1 - \mu)(\mu + x)}{(\mu + x)^2 + y^2 + z^2)^{3/2}} \\ 2y + \frac{-2\mu y}{(-1 + \mu + x)^2 + y^2 + z^2)^{-3/2}} - \frac{2(1 - \mu)y}{(\mu + x)^2 + y^2 + z^2)^{-3/2}} \\ \frac{-2\mu z}{(-1 + \mu + x)^2 + y^2 + z^2)^{-3/2}} - \frac{(1 - \mu)z}{((\mu + x)^2 + y^2 + z^2)^{-3/2}} \\ -2\dot{x} \\ -2\dot{y} \\ -2\dot{z} \end{bmatrix}. \tag{39}$$

The Jacobian of  $\mathbb{A}$  is simply

$$D\mathbb{A} = \pi \mathbf{Q}_R. \tag{40}$$

Finally, the Jacobian of  $T$  is

$$DT = \frac{1}{N_{npoints}} D\tau(\mathbf{X}_0) A_{\theta_0}, \tag{41}$$

where  $D\tau(\mathbf{X}_0)$  is given in Eq. (50).

#### 4.6 Numerical integration of the orbits

The RTBP is characterized by a nonstiff and smooth ordinary differential equations. For nonstiff problems, an explicit numerical integration technique achieves the desired accuracy with minimal computational costs. Additionally, for smooth ODEs, higher-order integration methods can be employed which further reduces the computation time. Thus, to numerically propagate the initial state variables, we used an explicit seventh-order Runge–Kutta method. The method integrates a system of ordinary differential equations using seventh-order Dormand and Prince formulas (Dormand and Prince 1981) and uses the the eighth-order results for adapting the step size.

#### 4.7 Numerical computation of the Poincaré map

The Poincaré map is defined in Eq. (7). The Poincaré section,  $\Sigma$ , given by  $g(\mathbf{x}) = 0$ , separates the phase space in two. Assuming that  $\Sigma$  is to be crossed in the direction from the initial

**Algorithm 3** Compute the Poincaré map

---

```

Input:  $X_0, f, h, tol, g, \nabla g$ 
 $t \leftarrow 0, \quad y \leftarrow X_0$ 
while  $g(y) * g(X_0) > 0$  do
   $rk87(f) := (t, y) \Rightarrow (t + h, y + \delta_y)$ 
   $t \leftarrow t + h, \quad y \leftarrow y + \delta_y$ 
end while
while  $|g(y)| > tol$  do
   $\delta = -g(y)/(\nabla g(y)f(y))$ 
   $rk87(f) := (t, y) \Rightarrow (t + \delta, y + \delta_y)$ 
end while
output:  $t, y.$ 

```

---

state's,  $\mathbf{X}_0$ , side of the phase space to the other side, Algorithm 3 is used to numerically obtain the Poincaré map. In the algorithm rk87 stands for the Runge–Kutta integration step.

Each iteration of the last loop corresponds to performing a Newton iteration to find a zero of the function  $F := g(\phi(\delta, y)) = 0$  with initial condition  $\delta = 0$ . In this case:

$$DF = \frac{dg}{d\phi(\delta, y)} \frac{d\phi(\delta, y)}{d\delta}. \quad (42)$$

Recalling the Euler integration formula,  $\phi(\delta, y) \approx y + f(y)\delta$ , we obtain  $DF = Dg(y)f(y)$ . It is possible to see that the pseudo-code employs root finding via the Newton iteration,  $\delta = -FDF^{-1}$ . At the end of the algorithm when the user set tolerance,  $tol$ , is achieved,  $P(\mathbf{X}_0) = y$  and  $\tau(\mathbf{X}_0) = t$ .

#### 4.8 Numerical computation of the first variation of the ODE

In order to find the derivative of the Poincaré map, we need to know how changes in the initial conditions of the ODE affect the final state to first order.

This can be achieved by looking at how much a perturbed trajectory  $\phi(t, \mathbf{x}_0 + \delta\mathbf{x}_0)$  separates from the periodic trajectory  $\phi(t, \mathbf{x}_0)$  after a time interval,  $t$ :

$$\delta\mathbf{x}(t) = \phi(t, \mathbf{x}_0 + \delta\mathbf{x}_0) - \phi(t, \mathbf{x}_0). \quad (43)$$

Expanding the right hand side of the equation into a Taylor series gives the approximation

$$\delta\mathbf{x}(t) = \frac{\partial\phi(t, \mathbf{x}_0)}{\partial\mathbf{x}_0}\delta\mathbf{x}_0 + \text{high order terms}. \quad (44)$$

In order to obtain it numerically, we note that the trajectory satisfies its own ODE,

$$\frac{d}{dt} \frac{\partial\phi(t, \mathbf{x}_0)}{\partial\mathbf{x}_0} = \mathbf{f}(\phi(t, \mathbf{x}_0)), \quad \text{with } \phi(0, \mathbf{x}_0) = \mathbf{x}_0. \quad (45)$$

Differentiating this equation with respect to  $\mathbf{x}_0$ , we obtain

$$\frac{d}{dt} \frac{\partial\phi(t, \mathbf{x}_0)}{\partial\mathbf{x}_0} = \mathbf{Df} \frac{\partial\phi(t, \mathbf{x}_0)}{\partial\mathbf{x}_0}. \quad (46)$$

where

$$\mathbf{Df} = \begin{pmatrix} \mathbf{0}_3 & \mathbf{I}_3 \\ \bar{U}_{x,x}^* & 2\Omega \end{pmatrix}, \quad (47)$$

and  $\mathbf{0}_3$  is the  $3 \times 3$  zero matrix,  $\mathbf{I}_3$  is the  $3 \times 3$  identity matrix,  $\bar{U}_{xx}^*$  is the matrix of symmetric second partial derivatives of  $\bar{U}$  with respect to  $x, y$  and  $z$ ,

$$\bar{U}_{xx}^* = \begin{pmatrix} \bar{U}_{xx} & \bar{U}_{xy} & \bar{U}_{xz} \\ \bar{U}_{yx} & \bar{U}_{yy} & \bar{U}_{yz} \\ \bar{U}_{zx} & \bar{U}_{zy} & \bar{U}_{zz} \end{pmatrix}, \tag{48}$$

and  $\Omega$  is given by

$$\Omega = \begin{pmatrix} 0 & 1 & 0 \\ -1 & 0 & 0 \\ 0 & 0 & 0 \end{pmatrix}. \tag{49}$$

We define  $D\phi := \frac{\partial \phi(t; \mathbf{x}_0)}{\partial \mathbf{x}_0}$  to be the first variation of the ODE. We note that,  $\frac{\partial \phi(0; \mathbf{x}_0)}{\partial \mathbf{x}_0} = \mathbf{I}_6$  by definition.

Now we define a new 42-dimensional augmented state vector consisting of the 6-dimensional state vector and the 36-dimensional first variation matrix:  $\mathbf{x}_{aug} = [\mathbf{x} ; D\phi(\cdot)]$  and integrating the augmented state vector with initial condition  $[\mathbf{x}_0 ; I(\cdot)]$  in order to obtain the first variation matrix.

#### 4.9 Numerical computation of the derivative of the Poincaré Map

The differential of the Poincaré map is computed as

$$\begin{aligned} DP(\mathbf{x}) &= \frac{d}{dx} \phi(\tau(\mathbf{x}), \mathbf{x}) = \frac{d}{d\tau} \phi(\tau(\mathbf{x}), \mathbf{x}) D\tau(\mathbf{x}) + D\phi(\tau(\mathbf{x}), \mathbf{x}) \\ &= \mathbf{f}(P(\mathbf{x})) D\tau(\mathbf{x}) + D\phi(\tau(\mathbf{x}), \mathbf{x}), \end{aligned} \tag{50}$$

where the differential of the time to reach  $\Sigma$  is obtained by differentiating the Poincaré section condition,

$$\begin{aligned} 0 &= g(P(\mathbf{x})) \\ \Rightarrow &= \nabla g(P(\mathbf{x})) DP(\mathbf{x}) \\ &= \nabla g(P(\mathbf{x})) [\mathbf{f}(P(\mathbf{x})) D\tau(\mathbf{x}) + D\phi(\tau(\mathbf{x}), \mathbf{x})] \\ &= [\nabla g(P(\mathbf{x})) \mathbf{f}(P(\mathbf{x}))] D\tau(\mathbf{x}) + \nabla g(P(\mathbf{x})) D\phi(\tau(\mathbf{x}), \mathbf{x}) \\ \Rightarrow D\tau(\mathbf{x}) &= - \frac{\nabla g(P(\mathbf{x})) D\phi(\tau(\mathbf{x}), \mathbf{x})}{\nabla g(P(\mathbf{x})) \mathbf{f}(P(\mathbf{x}))} \end{aligned} \tag{51}$$

Substituting Eq. (51) into Eq. (50), we obtain:

$$DP(\mathbf{x}) = -\mathbf{f}(P(\mathbf{x})) \frac{\nabla g(P(\mathbf{x})) D\phi(\tau(\mathbf{x}), \mathbf{x})}{\nabla g(P(\mathbf{x})) \mathbf{f}(P(\mathbf{x}))} + D\phi(\tau(\mathbf{x}), \mathbf{x}). \tag{52}$$

Recall that in this study two types of Poincaré sections are used. For the quasi-halo Poincaré section defined in Eq. (29),  $\nabla g$  is

$$\nabla g = \{ \dot{x}, \dot{y}, \dot{z}, 0, 0, 0 \}^T, \tag{53}$$

and for the Lissajous Poincaré section defined in Eq. (27),

$$\nabla g = \{ 0, 0, 1, 0, 0, 0 \}^T. \tag{54}$$

#### 4.10 Continuation

For the quasi-halo continuation with both the constant Jacobi energy and the constant period cases, we used the area,  $\mathbb{A}$ , of the projection of the invariant circle on the Poincaré section to the  $\dot{y} - \dot{z}$  plane as the continuation parameter in accordance with the choice  $\theta = \tan^{-1}(\dot{z}/\dot{y})$ . For the Lissajous orbit continuation with the constant Jacobi energy case, we used the area,  $\mathbb{A}$ , of the projection of the invariant circle on the Poincaré section in the  $x - y$  plane as the continuation parameter in accordance with the choice  $\theta = \tan^{-1}(y/x)$ . For the first continuation, we used a linear extrapolation starting from  $\mathbf{Q}_0$  to find  $\mathbf{Q}_1$ . For the second and third continuations, we used a second- and third-order polynomial fit to extrapolate the value of  $\mathbf{Q}$ . From the fourth continuation onwards, we used a fourth-order polynomial fit to extrapolate the value of  $\mathbf{Q}$  from the known values. Higher-order polynomial fits were avoided due to the well-known Runge's phenomenon, which leads to wildly oscillating interpolating function (Boyd and Xu 2009).

First, we obtain the polynomial fit:

$$\text{polyfunc}(\mathbb{A}) = \text{polyfit}([\mathbf{Q}_k, \mathbf{Q}_{k-1}, \dots, \mathbf{Q}_0, \mathbf{0}], [\mathbb{A}_k, \mathbb{A}_{k-1}, \dots, \mathbb{A}_0, 0], \mathbb{O}) \quad (55)$$

where *polyfit* is the usual least square polynomial fit of degree  $\mathbb{O}$ . Then, the continuation of the Fourier coefficient is performed by extrapolation:

$$\mathbf{Q}_{k+1} = \text{polyfunc}(\mathbb{A}_{k+1}), \quad (56)$$

where

$$\mathbb{A}_{k+1} = \mathbb{A}_k + \Delta\mathbb{A}. \quad (57)$$

While choosing  $\Delta\mathbb{A}$ , there is compromise between speed and convergence. The larger the  $\Delta\mathbb{A}$ , the shorter the continuation procedure takes, while the possibility of non-convergence increases with increasing step size. To find the optimal iteration step size automatically, we set

$$\Delta\mathbb{A} = \begin{cases} 1.2 \Delta\mathbb{A} & \text{if Newton iteration converged for all previous cases} \\ 0.8 \Delta\mathbb{A} & \text{if Newton iteration did not converge: repeat the previous step} \\ \Delta\mathbb{A} & \text{otherwise.} \end{cases}$$

Thus, when the iteration is convergent, increasingly large steps are taken to speed up the process, until the maximum step size is exceeded and the algorithm becomes divergent. Then, the step size is reduced and the iteration is continued with the optimal step size.

Finally, since  $\mathbb{A} \rightarrow 0$  implies  $\mathbf{Q} \rightarrow \mathbf{0}$  if  $\mathbb{A} = 0$  then  $\mathbf{Q} = \mathbf{0}$ . We used this property in the initial step of the continuation by initializing  $\Delta\mathbb{A} = \mathbb{A}_0$ .

Figure 9 shows how the first four elements of  $\mathbf{Q}$  vary with the continuation parameter for the quasi-halo family with a constant Jacobi energy.

## 5 Results

The four-dimensional center manifold around L2 is occupied by quasiperiodic orbits of two different families: the Lissajous family around the vertical Lyapunov orbits, and the quasi-halo orbits around the halo orbits. These quasiperiodic orbits reside on invariant tori about the corresponding periodic orbit.

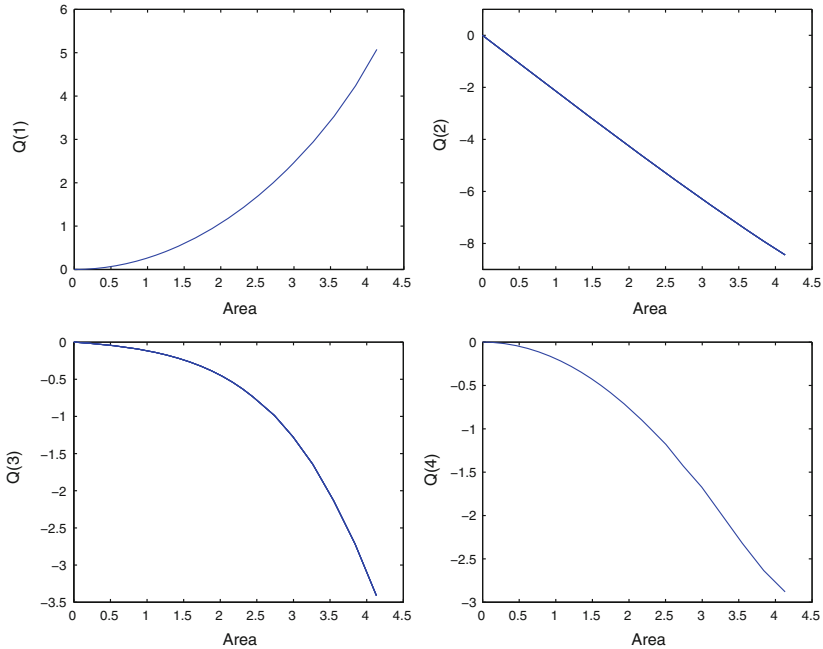


**Fig. 9** The first four elements of  $\mathbf{Q}$  for the constant Jacobi energy quasi-halo family versus the continuation variable area,  $\mathbb{A}$

In this section, we apply the multiple Poincaré section numerical method to find these orbits. Once the Fourier coefficients on the Poincaré sections are obtained as described in the previous section, the two-dimensional quasiperiodic orbit is obtained by integrating a sample point on one of the Poincaré sections until it crosses the same section again. Due to error bounds on the multiple Poincaré section algorithm, this intersection point is very close to, but not exactly on, the one-dimensional invariant circle. This point is projected onto the invariant circle by finding  $\theta_{proj} = \tan^{-1}(y/x)$  or  $\theta_{proj} = \tan^{-1}(\dot{z}/\dot{y})$ , depending on whether the point is on a quasi-halo or on a Lissajous orbit. Then the projected point  $X_{proj} = A_{\theta_{proj}} \mathbf{Q}$  is integrated, as with the initial sample point, until it crosses the Poincaré section, and the procedure is repeated for the desired period length. Finally, these solutions are concatenated to obtain the full orbit.

The full Lissajous family was obtained numerically via the multiple Poincaré section method, as shown in Fig. 3. Figure 10 shows typical Lissajous orbits around the L2 point.

The full quasi-halo family was obtained via multiple Poincaré section method, as shown in Fig. 3. Figure 11 shows typical quasi-halo orbits around the L2 point.

### 5.1 Comparison of the results with the literature

The Poincaré section based on orbital period, where we specified the orbit period along the halo, is shown in Fig. 12. Here, the results are compared to Gómez et al. (1999). The main advantage of the Poincaré sections approach is the execution speed. The calculations take only a few minutes of computation time, with minimal programming requirement.

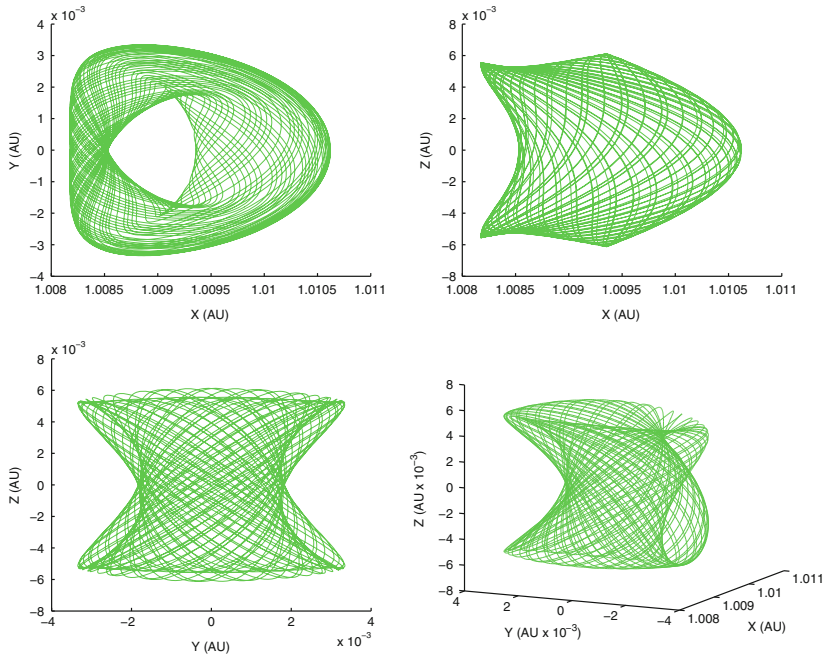


**Fig. 10** Example of a Lissajous Orbit around L2

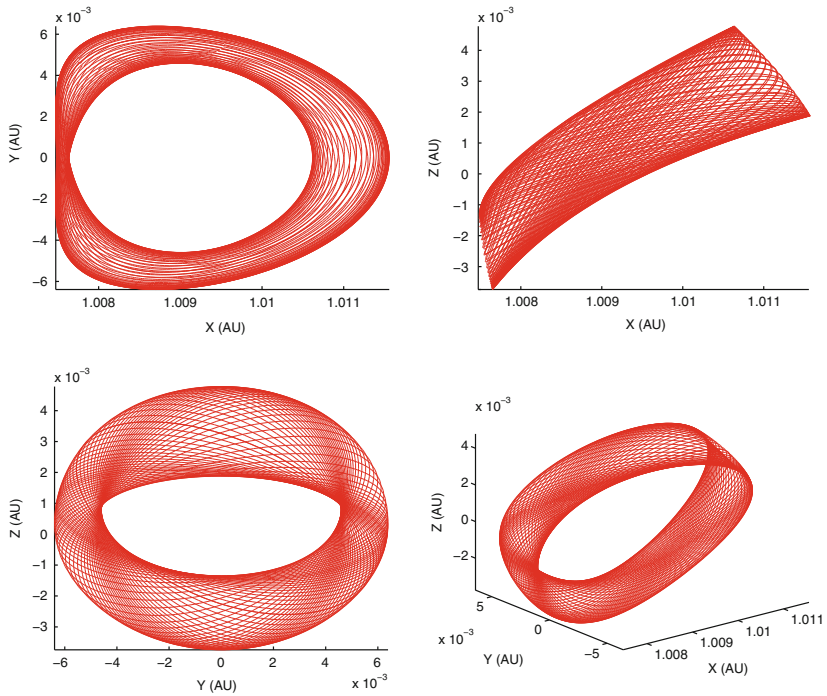


**Fig. 11** Example: Quasi-halo orbit around L2

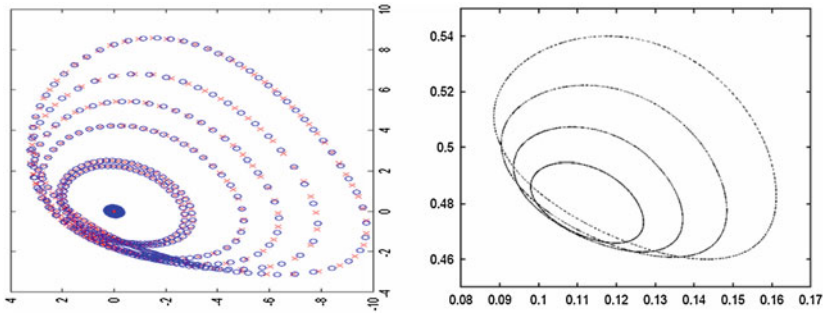


**Fig. 12** The Poincaré section of the invariant tori, where the period of all orbits is equal to that of the base halo orbit. The multiple Poincaré sections method is shown on the *left*, while the Lindstedt-Poincaré method is shown on the *right* Gómez et al. (1999)

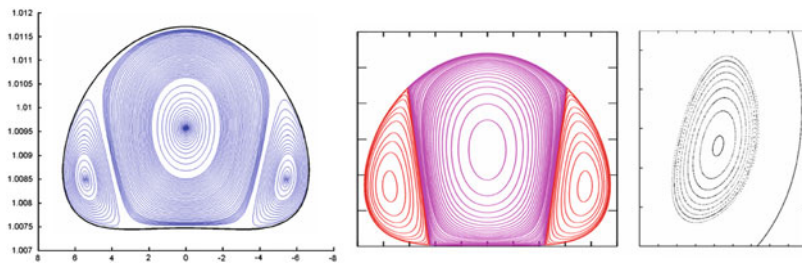


**Fig. 13** The Poincaré section of the complete quasiperiodic family around L2 with energy that is equivalent to the 500,000 km-sized halo orbit on the ecliptic plane (on the *left*). Similar results from Gómez and Mondelo (2001), Mondelo (2001) (in the *middle*) and Gómez et al. (1999) (on the *right*)

Utilizing the multiple sections approach, the complete quasiperiodic orbit families around the libration points are found. Figure 13 shows the Poincaré section of the quasiperiodic family with constant energy on the ecliptic plane, comparing the results obtained by our multiple Poincaré sections method with Gómez and Mondelo’s refined Fourier analysis (Gómez and Mondelo 2001; Mondelo 2001) and Gómez et al.’s Lindstedt-Poincaré analysis (Gómez et al. 1999). While the Lindstedt-Poincaré analysis Gómez et al. (1999) cannot obtain the complete families and a cluster of parallel computers was required to get the complete families with the refined Fourier analysis (Gómez and Mondelo 2001; Mondelo 2001), our method obtains the complete set of quasiperiodic orbits with a computation time (for the full families) of only three minutes on a 2.15 GHz Intel Pentium processor.

## 6 Extension to the full ephemeris

Since the RTBP is a good first-order approximation to the real Solar System dynamics, there are orbits in the Solar System that have very similar shapes and properties to the orbits found in the simplified model. The aim of this section is to find these orbits.

We take the real Solar System dynamics to be the point-mass gravitational interactions of the major Solar System bodies given at each time-instant by the JPL DE-406 ephemeris, which is the latest version of the JPL Solar System ephemeris (Standish 1998). It specifies the past and future positions of the Sun, the Moon, and the planets in the three-

dimensional space with respect to the Solar System barycenter. The ephemeris gives the Chebyshev polynomial coefficients corresponding to the J2000 epoch positions of these Solar System bodies (Standish 1998, 1982). In the calculations to follow, oblateness and tri-axiality of the planets is not taken into account. Solar radiation pressure effects are neglected as well.

The purpose is to find full-ephemeris orbits that have the same characteristics as the quasi-periodic orbits found using the RTBP model. Thus, the algorithm first takes the orbits in the RTBP and converts them from the synodical frame to the heliocentric frame.

We used the usual synodical frame, which has its origin at the center-of-mass of the Sun–Earth/Moon Barycenter system, to map the RTBP results to the full ephemeris model. However, the large distance between the Sun and the spacecraft leads to undesirable behavior. Multiplying small errors by this large distance leads to non-convergent trajectories. Thus, we moved the position of the coordinate system from the center-of-mass of the Sun–Earth/Moon Barycenter system, to the Earth/Moon Barycenter.

In what follows, the subscripts *cm*, *syn*, *sun*, *em*, and *e/s* refer, respectively, to the center-of-mass of the Solar System, the synodical frame, the Sun, the Earth/Moon Barycenter, and the Earth/Moon Barycenter with respect to the Sun. The superscripts *R* and *I* refer to the rotating and the inertial coordinates.  $\mathbf{r}$  and  $\mathbf{v}$  are the position and velocity vectors of the spacecraft. Finally,  $\mathbf{R}$  and  $\mathbf{V}$  are the position and velocity vectors of the Solar System bodies with respect to the Solar System center-of-mass, unless specified otherwise.

First, the following relation is obtained from DE-406:

$$\mathbf{R}_{e/s} = \mathbf{R}_{em} - \mathbf{R}_{sun}. \quad (58)$$

The position, velocity and angular velocity of the rotating frame are calculated:

$$\mathbf{R}_{cm} = \mathbf{R}_{em}, \quad \mathbf{V}_{cm} = \mathbf{V}_{em}, \quad \boldsymbol{\omega} = \frac{\mathbf{R}_{e/s} \times \mathbf{V}_{e/s}}{|\mathbf{R}_{e/s}|^2}. \quad (59)$$

Then,  $(1 - \mu)$  is subtracted from the x-axis of the synodical frame position vector to find the distance to the new origin at the Earth/Moon barycenter, and the synodical quantities are multiplied by the length and time scale to re-dimensionize the coordinates:

$$\begin{aligned} \mathbf{r}_{syn}^R &= \|\mathbf{R}_{e/s}\| \left( \mathbf{r}_{syn}^R - [1 - \mu, 0, 0]^T \right), \\ \mathbf{v}_{syn}^R &= \|\mathbf{R}_{e/s}\| \|\boldsymbol{\omega}\| \mathbf{v}_{syn}^R. \end{aligned} \quad (60)$$

The rotation matrix from the synodical frame to the inertial frame,  $\mathcal{R} = [\hat{\mathbf{e}}_1 \ \hat{\mathbf{e}}_2 \ \hat{\mathbf{e}}_3]$ , is calculated as follows

$$\hat{\mathbf{e}}_1 = \frac{\mathbf{R}_{e/s}}{\|\mathbf{R}_{e/s}\|}, \quad \hat{\mathbf{e}}_3 = \frac{\boldsymbol{\omega}}{\|\boldsymbol{\omega}\|}, \quad \text{and} \quad \hat{\mathbf{e}}_2 = \frac{\hat{\mathbf{e}}_3 \times \hat{\mathbf{e}}_1}{\|\hat{\mathbf{e}}_3 \times \hat{\mathbf{e}}_1\|}. \quad (61)$$

The synodical coordinates are expressed in inertial frame coordinates:

$$\mathbf{r}_{syn}^I = \mathcal{R} \mathbf{r}_{syn}^R, \quad \mathbf{v}_{syn}^I = \mathcal{R} \mathbf{v}_{syn}^R. \quad (62)$$

Finally, the inertial position,  $\mathbf{r}_{solar}^I$ , and velocity,  $\mathbf{v}_{solar}^I$ , of the spacecraft are found with respect to the Solar System center-of-mass:

$$\begin{aligned} \mathbf{r}_{solar}^I &= \mathbf{r}_{syn}^I + \mathbf{R}_{cm}, \\ \mathbf{v}_{solar}^I &= \mathbf{v}_{syn}^I + \boldsymbol{\omega} \times \mathbf{r}_{syn}^I + \mathbf{V}_{cm}. \end{aligned} \quad (63)$$

Once the positions and velocities are mapped to Solar System coordinates, we take these orbits as initial guesses, and find the natural orbits in the full ephemeris model that remain close to them. Our approach is to take an orbit for a specified time interval, which would be the time frame of the mission, and to feed this guess into a collocation algorithm.

The aim of the collocation algorithm is to find the orbits in the full ephemeris model that stay close to the RTBP solutions found previously. We utilize the collocation algorithm to discretize the first-order differential equation to a set of difference equations at discrete times,  $t_i$ , and the corresponding discrete states  $x_i := x(t_i)$  as follows

$$\dot{\mathbf{x}}(t) - \mathbf{f}(t, \mathbf{x}) = 0 \Rightarrow \mathbb{F}(t_i, \mathbf{x}_i, t_{i+1}, \mathbf{x}_{i+1}) = 0. \tag{64}$$

There are many schemes that can be used for this discretization. Among the most popular are the Runge–Kutta formulas and Simpson’s quadrature. Cash and Wright developed the TWBVP algorithm (Cash and Wright 1990, 1991), in which the basic formula is Simpson’s rule. In the BVP solver COLNEW, Ascher et al. (1981, 1988), implemented a family of implicit Runge–Kutta methods.

We implemented the Simpson’s formula for the quadrature as given by Kierzenka and Shampine (2001). One advantage of this implementation is that the discretized equations can be analytically solved without intermediate variables. If the initial guess is sufficiently close to the real solution, the discretized Simpson quadrature equation, which corresponds to the differential equation, gives the following constraint at every point:

$$\begin{aligned} \mathbb{F}(t_i, \mathbf{x}_i, t_{i+1}, \mathbf{x}_{i+1}) = & -\mathbf{x}_{i+1} + \mathbf{x}_i + \frac{h_i}{6} (\mathbf{f}(t_i, \mathbf{x}_i) + \mathbf{f}(t_{i+1}, \mathbf{x}_{i+1})) \dots \\ & + \frac{2h_i}{3} \mathbf{f} \left( \frac{t_i + t_{i+1}}{2}, \frac{\mathbf{x}_i + \mathbf{x}_{i+1}}{2} - \frac{h_i}{8} [\mathbf{f}(t_i, \mathbf{x}_i) - \mathbf{f}(t_{i+1}, \mathbf{x}_{i+1})] \right), \end{aligned} \tag{65}$$

where  $h_i = t_{i+1} - t_i$ .

Without adding any boundary conditions, we solve the  $N$ -dimensional nonlinear equation given by  $\mathbb{F} = 0$ , using Newton’s method, following Kierzenka et al.’s *bvp4c* implementation (Kierzenka and Shampine 2001). Thus, without any constraints, we look for an orbit that satisfies the full Solar System ODE, starting with the initial guess obtained from the RTBP. The result is a natural orbit of the Solar System, which is very close in shape and characteristics to the RTBP orbit.

Finally, for visualization purposes, the results in the solar coordinates are converted back to the synodical frame by applying the algorithm backwards. Figures 14, 15, and 16 show the results for three different types of orbits—halo, quasi-halo and Lissajous—around the Sun–Earth L2 point, transitioned to the JPL DE-406 model. These orbits all have the same base halo orbit.

The collocation algorithm performs robustly around the Sun–Earth L2 point where the missions of interest might be located. We also implemented the multiple shooting algorithm, developed by Gómez et al. (1999) for the quasi-halo refinement for comparison. The obtained results and the computation time from both methods are similar. However, the multiple shooting method is known to have convergence issues for the more computationally challenging Earth–Moon system orbits and robustness of the collocation algorithm may be an advantage in these orbits. Convergence comparison for more challenging cases will be performed as part of future research.

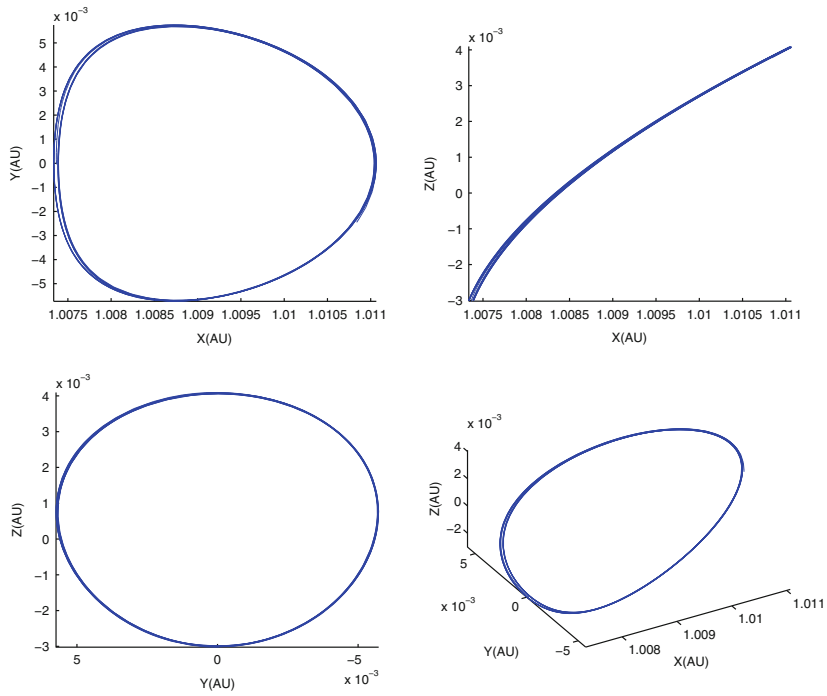


**Fig. 14** An example of a halo orbit around L2 transitioned to the JPL DE-406 model

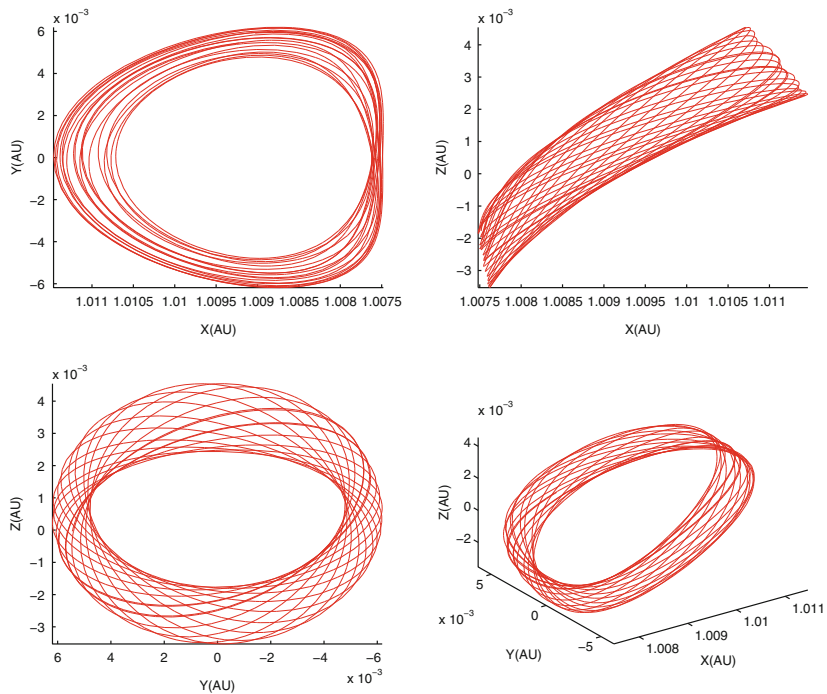


**Fig. 15** An example of a quasi-halo orbit around L2 transitioned to the JPL DE-406 model

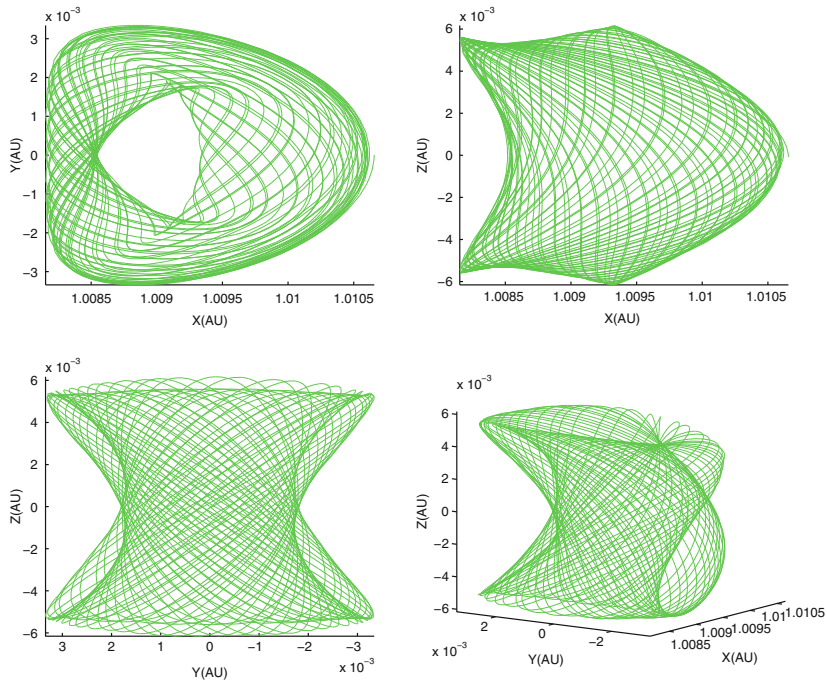


**Fig. 16** An example of a Lissajous orbit around L2 transitioned to the JPL DE-406 model

## 7 Conclusions

This paper developed a computationally efficient, stable, easy-to-implement, and accurate multiple-Poincaré-sections method to find quasiperiodic orbits. This method enabled specification of the period, size and energy of the quasiperiodic orbit. A continuation method to expand the results from a single solution to a family of orbits was introduced. Quasi-halo and Lissajous families around the L2 libration point were obtained via this method. A numerical method to transform these orbits from the RTBP model to the real ephemeris model of the Solar System was introduced and applied. The results compare favorably with the existing literature in terms of computational time, and ease and flexibility of implementation.

## References

- Ascher, U., Christiansen, J., Russell, R.D.: Collocation software for boundary-value ODEs. *ACM Trans. Math. Softw.* **7**, 209–222 (1981)
- Ascher, U., Mattheij, R.M.M., Russell, R.D.: *Numerical Solution of Boundary Value Problems for Ordinary Differential Equations*. Prentice-Hall, Englewood Cliffs, NJ (1988)
- Barden, B.T., Howell, K.C.: Formation flying in the vicinity of libration point orbits. *Adv. Astronaut. Sci. Spacefl. Mech.* **99**, 969–989 (1998)
- Barden, B.T., Howell, K.C.: Dynamical issues associated with relative configurations of multiple spacecraft near the Sun–Earth/Moon L1 point. *Adv. Astronaut. Sci. Astrodyn.* **103**, 2307–2327 (1999)
- Boyd, J.P., Xu, F.: Divergence (Runge Phenomenon) for least-squares polynomial approximation on an equispaced grid and Mock-Chebyshev subset interpolation. *Appl. Math. Comput.* **210**(1), 158–168 (2009)
- Breakwell, J.V., Brown, J.: The Halo family of three dimensional periodic orbits in the Earth–Moon restricted three body problem. *Celest. Mech.* **20**(4), 389–404 (1979)

- Cash, J.R., Wright, M.H.: Implementation issues in solving nonlinear equations for two-point boundary value problems. *Computing* **55**, 17–37 (1990)
- Cash, J.R., Wright, M.H.: A deferred correction method for nonlinear two-point boundary value problems: implementation and numerical evaluation. *SIAM J. Sci. Stat. Comput.* **12**, 971–989 (1991)
- Dormand, J.R., Prince, P.J.: High order embedded Runge-Kutta formulae. *J. Comput. Appl. Math.* **7**(1), 67–75 (1981)
- Farquhar, R.W.: Lunar Communications with Libration-Point Satellites. *J. Spacecr. Rocket.* **4**(10), 1383–1384 (1967)
- Farquhar, R.W., Kamel, A.A.: Quasi-periodic orbits about the translunar libration point. *Celest. Mech.* **7**(4), 458–473 (1973)
- Gómez, G., Jorba, A., Masdemont, J.J., Simó, C.: Dynamics and Mission Design Near Libration Point Orbits—Volume 3: Advanced Methods for Collinear Points. World Scientific, Singapore (2000)
- Gómez, G., Koon, W.S., Lo, M.W., Marsden, J.E., Masdemont, J., Ross, S.D.: Connecting orbits and invariant manifolds in the spatial restricted three-body problem. *Nonlinearity* **17**, 1571–1606 (2004)
- Gómez, G., Llibre, J., Martínez, R., Simó, C.: Dynamics and Mission Design Near Libration Point Orbits—Volume 1: Fundamentals: The Case of Collinear Libration Points. World Scientific (2000)
- Gómez, G., Masdemont, J.J., Simó, C.: Quasihalo orbits associated with libration points. *J. Astronaut. Sci.* **46**(2), 1–42 (1999)
- Gómez, G., Mondelo, J.M.: The dynamics around the collinear equilibrium points of the RTBP. *Physica D* **157**(4), 283–321 (2001)
- Hénon, M.: Vertical stability of periodic orbits in the restricted problem I. Equal Masses. *Astron. Astrophys.* **28**, 415–426 (1973)
- Howell, K.C.: Three dimensional periodic Halo orbits. *Celest. Mech.* **32**(1), 53–72 (1984)
- Howell, K.C., Pernicka, H.J.: Numerical determination of Lissajous trajectories in the restricted three-body problem. *Celest. Mech.* **41**(1–4), 107–124 (1988)
- Jorba, A., Masdemont, J.J.: Dynamics in the center manifold of the restricted three-body problem. *Physica D* **132**, 189–213 (1999)
- Jorba, A., Villanueva, J.: Numerical computation of normal forms around some periodic orbits of the restricted three body problem. *Physica D* **114**, 197–229 (1998)
- Kevrekidis, I.G., Aris, R., Schmidt, L.D., Pelikan, S.: Numerical computations of invariant circles of maps. *Physica D* **16**, 243–251 (1985)
- Kierzenka, J., Shampine, L.F.: A BVP solver based on residual control and the matlab PSE. *ACM Trans. Math. Softw.* **27**(3), 299–316 (2001)
- Mondelo, J.M.: Contribution to the Study of Fourier Methods for Quasi-Periodic Functions and the Vicinity of the Collinear Libration Points. PhD thesis, Universitat de Barcelona, Departament de Matemàtica Aplicada i Anàlisi (2001)
- Murray, C.D., Dermott, S.F.: *Solar System Dynamics*. Cambridge University Press, Cambridge (2000)
- Rayleigh, J.W.S.: On the Character of the Complete Radiation at a Given Temperature. *Philos. Mag.* **27**, 460–469 (1806)
- Schilder, F., Osinga, H.M., Vogt, W.: Continuation of quasi-periodic invariant tori. *SIAM J. Appl. Dyn. Syst.* **4**(3), 459–488 (2005)
- Standish, E.M.: JPL Planetary and Lunar Ephemerides, DE405/LE405. JPL IOM, 312.F-98-048 (1998)
- Standish, E.M.: Orientation of the JPL Ephemerides, DE200/LE200, to the Dynamical Equinox of J 2000. *Astron. Astrophys.* **114**, 297–302 (1982)